JGR Solid Earth

RESEARCH ARTICLE
10.1029/2022JB025624

Key Points:

- CO_2 environment reduces maximum yield stress of quartz by 10% and fracture toughness by 12.1% compared to quartz in vacuum
- Crack initiation mechanism is affected by CO_2: voids form at low strain due to pressure build-up by physisorbed molecules on crack surface
- Corrosive impact of CO_2 environment diminishes at slower strain rates

Supporting Information:

Supporting Information may be found in the online version of this article.

Correspondence to:

F. Simeski,
filip.simeski@stanford.edu

Citation:

Simeski, F., & Ihme, M. (2023). Corrosive influence of carbon dioxide on crack initiation in quartz: Comparison with liquid water and vacuum environments. *Journal of Geophysical Research: Solid Earth*, *128*, e2022JB025624. https://doi.org/10.1029/2022JB025624

Received 14 SEP 2022
Accepted 11 JAN 2023

Author Contributions:

Conceptualization: Filip Simeski, Matthias Ihme
Data curation: Filip Simeski
Formal analysis: Filip Simeski
Funding acquisition: Matthias Ihme
Investigation: Filip Simeski, Matthias Ihme
Methodology: Filip Simeski
Project Administration: Matthias Ihme
Resources: Matthias Ihme
Software: Filip Simeski
Supervision: Matthias Ihme
Validation: Filip Simeski
Visualization: Filip Simeski
Writing – original draft: Filip Simeski, Matthias Ihme
Writing – review & editing: Filip Simeski, Matthias Ihme

Corrosive Influence of Carbon Dioxide on Crack Initiation in Quartz: Comparison With Liquid Water and Vacuum Environments

Filip Simeski[1] and Matthias Ihme[1,2]

[1]Department of Mechanical Engineering, Stanford University, Stanford, CA, USA, [2]SLAC National Accelerator Laboratory, Menlo Park, CA, USA

Abstract The stimulation of crack growth in quartz and siliceous materials by injecting carbon dioxide (CO_2) represents a key technology in long-term carbon storage and in the development of natural gas wells. While this technology is widely used, the molecular impact of CO_2 interactions on the solid matrix is only incompletely understood. In this work, we employ reactive molecular dynamics simulations to study how the CO_2 fluid environment affects the mechanical properties of pre-cracked single-crystal quartz. The thermodynamic conditions of interest are those relevant to subsurface reservoirs. We report how structural properties of quartz—bond length distribution and crack tip shape—evolve upon introduction of a fluid. These properties are directly related to macroscopic quantities of the global stress–strain curves, thus reaffirming the inherent coupling across multiple scales for fluid–solid interactions in the subsurface. We find that CO_2 reduces the fracture toughness of quartz by 12.1% compared to that of quartz in vacuum, thereby promoting crack growth and enhancing fluid transport in the subsurface.

Plain Language Summary Exposing mineral surfaces to chemical environments impacts their mechanical properties. Many subsurface engineering applications expose quartz, which is one of the most common minerals in Earth's subsurface, to high-pressure carbon dioxide (CO_2). While previous research has probed the impact of polar fluids on the mechanical properties of quartz, the influence of CO_2 on these properties is incompletely understood. Employing reactive molecular dynamics simulations, we study crack initiation in quartz exposed to CO_2 and quantify its mechanical and structural properties. The CO_2 environment reduces the fracture toughness of quartz by 12.1% compared to quartz in vacuum, effectively making the material less resistant to growth of flaws, such as cracks. In subsurface reservoirs, the growth of cracks enhances fluid transport. Our findings may be used for development and calibration of constitutive models of quartz exposed to CO_2, including applications to geologic carbon storage.

1. Introduction

Understanding how a carbon dioxide (CO_2) bath affects the mechanical properties of quartz is critical for a number of engineering applications, including geologic carbon storage (Benson & Cole, 2008) and enhanced gas recovery from shale formations (Oldenburg et al., 2001). Both of these processes depend on the injection of fluids, including CO_2, into the subsurface rock matrix. Once CO_2 is injected into these formations, it interacts with the minerals and rocks via coupled thermal-hydrological-mechanical-chemical processes (Taron & Elsworth, 2009; Zhang et al., 2016), including adsorption, reaction, and crack propagation. One such process is stress corrosion cracking (Raja & Shoji, 2011), which is recognized to be the main mechanism for fracture growth in the upper crust of the Earth (Laubach et al., 2019). At the nanoscale, localized imperfections in the solid matrix can grow into fractures releasing trapped gas and increasing the connectivity of the pore network (Rahimi-Aghdam et al., 2019). Significant progress has been made toward understanding the effects of stress corrosion on metal alloys (Raja & Shoji, 2011). However, the molecular mechanism triggering stress corrosion is not well understood for the complex environment of subsurface reservoirs (Jew et al., 2022; Laubach et al., 2019). To shed light on this mechanism, we perform reactive molecular dynamics (MD) simulations that examine the effects of CO_2 on crack initiation in quartz (SiO_2). Moreover, we identify trends in the corrosive influence by varying the applied strain rate. Finally, the fracture toughness of quartz is calculated at reservoir-relevant conditions.

Shale rock, which constitutes unconventional formations, is a material with low permeability and highly heterogeneous composition. Stress corrosion has been identified for common clays and minerals occurring in shale,

such as quartz (Rimsza et al., 2018b), calcite (Henry et al., 1977), and a number of other rock types (Laubach et al., 2019; Meredith & Atkinson, 1983). Ternary diagrams show siliceous compounds, such as quartz and feldspar, form a prominent share of the solid matrix in shales (Chermak & Schreiber, 2014). Therefore, quartz and silica are often used as model systems for shale rock in experimental and computational studies (Atkinson & Meredith, 1987; Barsotti et al., 2016; Coasne et al., 2013). The fracture toughness and mechanical properties of silica have been well-characterized through experiments for a wide range of length scales (Bruns et al., 2020; Wiederhorn & Bolz, 1970; Yue & Zheng, 2014). These properties are often input to continuum models to predict macroscopic fracture growth. A few MD studies have investigated the onset of and mechanism for crack propagation at the nanoscale. Rimsza et al. (2018b) used reactive MD simulations to examine subcritical crack growth in amorphous silica in vacuum and found that a process zone develops in radius of 1.5 nm around the crack tip, in agreement with experimental measurements. The same approach was adopted to explore the impact of boundary and loading conditions on mechanical properties (Vo, Reeder, et al., 2020), which led to a set of guidelines to obtain reproducible properties for amorphous silica. By investigating tensile rupture of α-quartz in vacuum, Guren et al. (2022) observed crack path instabilities at speeds greater than 15% of the Rayleigh wave speed.

Beyond the studies of mechanical properties in vacuum and air, the evolution of these properties has been investigated in water (H_2O) and aqueous solutions. The role of fluid acidity in stress corrosion was experimentally examined by Atkinson and Meredith (1981). They concluded that crack growth in quartz is enhanced proportionally with the hydroxide concentration of the aqueous environment. This relationship was later translated into a molecular mechanism for stress corrosion in the presence of water (Michalske & Freiman, 1982). Computational studies of the water–silica system showed that stress corrosion can lower the fracture toughness by up to ∼25% (Rimsza et al., 2018a).

Michalske and Freiman (1982) developed a molecular mechanistic model to describe effects of H_2O on crack propagation in quartz. However, this model accounts only for polar fluids. Many engineering applications require the corrosive impact of non-polar fluids, namely CO_2, on quartz to be predicted. In this work, we propose a molecular mechanism for the corrosive influence of CO_2 on quartz and show that this process leads to 12.1% average reduction in fracture toughness. Complementary simulations in vacuum and in H_2O serve as a reference for comparison of the properties and mechanism observed in the CO_2 environment. Lower applied strain rate further reduces the mechanical properties by allowing for relaxation of the process zone in the quartz sample. This impact is quantified for each of the three environments studied: vacuum, H_2O, and CO_2.

2. Computational Methods

The system dynamics were calculated with the Large-scale Atomic/Molecular Massively Parallel Simulator (LAMMPS) (LAMMPS Manual, 2022; Plimpton, 1995). To describe the charge transfer and reactivity at the crack tip, a reactive force field (Aktulga et al., 2012) was employed via the ReaxFF parameters of Fogarty et al. (2010). Cowen and El-Genk (2016) demonstrated that this force field recovers properties of quartz within ∼5% of experimental measurements. Furthermore, we assessed the performance of this force field in predicting the CO_2–quartz interactions by comparing ReaxFF MD results to the adsorption energy of CO_2 from density functional theory calculations and to the transverse density profiles from non-reactive MD simulations. These comparisons are presented in the Supporting Information S1. As expected for nanoconfined CO_2, the transverse density profiles show that an adsorption layer with enhanced density forms near quartz surfaces due to fluid–solid interactions.

We present results based on three different sets of simulations: (a) dry quartz, (b) H_2O corrosion, and (c) CO_2 corrosion. The dry quartz simulations, which are done in vacuum, study the crack initiation due to purely mechanical loading. The pure H_2O and pure CO_2 corrosion simulations study the combined effect of chemical and mechanical loading on crack initiation. In all simulations the α-quartz sample is $14 \times 14 \times 2.1$ nm^3 in size. These dimensions were selected based on findings in the literature about finite size effects when studying the mechanical properties of silica via MD (Vo, Reeder, et al., 2020), which we confirmed with a convergence study (see Supporting Information S1). To initialize the crack, all bonds are removed between the edge of the sample and 4.5 nm in the y-direction midplane parallel to the x–z plane. The crack is along the (001) surface of α-quartz. The sample was strained in a mode I tensile loading to open the crack, as shown in Figure 1. Energy minimization and a microcanonical ensemble simulation were adopted to relax the sample.

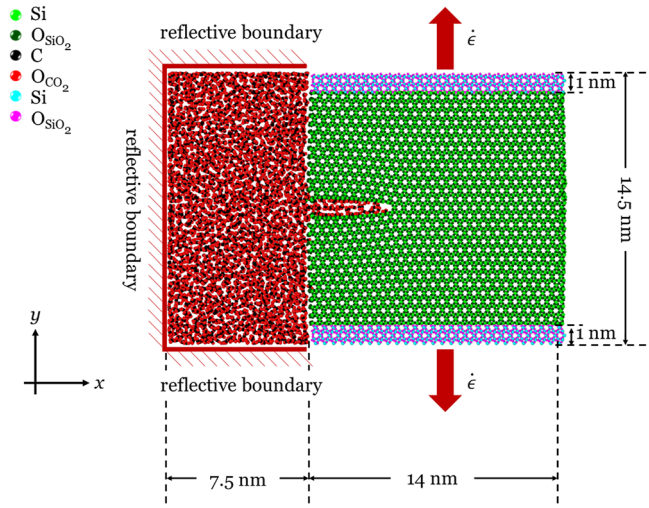

Figure 1. Setup of the molecular simulations. The quartz sample with the pre-opened crack is located next to a fluid reservoir. The reservoir is bounded by reflective walls to maintain fluid pressure. The sample is loaded mechanically via a prescribed velocity to the top and bottom 1-nm portions (atoms colored in cyan and magenta) of the quartz sample.

Once the crack was opened, fluid was introduced in a reservoir with dimensions 7.5 × 14.5 × 2.1 nm^3, adjacent to the cracked side of the α-quartz sample. For further loading, the atoms belonging to the top and bottom 1 nm of the sample in the y-direction were prescribed with a constant velocity. All other atoms in the simulation evolved according to canonical ensemble dynamics at 300 K. The dynamics were simulated until catastrophic failure occurred, that is, the crack propagated through the sample in the x-direction. The total simulation time varied with strain rate and fluid environment; and, it obtained values between 1.7 and 17 ns. The strain rates of interest were selected to be comparable with the diffusive crack filling rates and ranged between 3.4×10^6 and 3.4×10^7 s^{-1}. These strain rates are at least three orders of magnitude lower than those investigated in other MD studies that simulated the mechanical behavior of silica by applying strain (Chowdhury et al., 2016; Vo, Reeder, et al., 2020; Vo, He, et al., 2020).

Initially the fluid reservoir is at 100 atm and 300 K. To maintain the fluid density as the quartz sample is strained, reflective walls were introduced at the top, bottom, and left-hand-side boundaries of the reservoir. One limitation of this method is that the density of the reservoir decreases as the crack grows and fluid fills the newly opened volume. The change in density due to this process was estimated to be less than 10%. To obtain statistically relevant results, at the highest strain rate studied we ran three replica simulations with different initial molecular configurations. The presented results are ensemble averaged over these simulations.

In post-processing the MD data, we assume linear elastic fracture mechanics (LEFM), which is consistent with other MD studies (Rimsza et al., 2018a). Based on LEFM theory, the stress intensity factor, K_I, is evaluated from the crack plane normal stress, σ (Tada et al., 2000):

$$K_I = \sigma\sqrt{\pi l_c}\sum_{i=0}^{4}\alpha_i\left(\frac{l_c}{l_s}\right)^i \quad (1)$$

with $\alpha_0 = 1.122$, $\alpha_1 = -0.231$, $\alpha_2 = 10.55$, $\alpha_3 = -21.71$, and $\alpha_4 = 30.382$. In this expression, $l_c = 4.5$ nm is the length of the pre-existing crack and $l_s = 14$ nm is the sample length. The fracture toughness, K_{IC}, is given by the critical value of the stress intensity factor.

3. Results and Discussion

The goal of this paper is to quantify the corrosive influence of CO_2 on crack initiation in α-quartz. To achieve this goal, we considered a single-crystal quartz that is pre-cracked and located next to a reservoir of pure CO_2 at 100 atm. In this model system, we assumed an atomistic crack tip and we examined a number of mechanical properties from the reactive MD data in the context of LEFM. Global stress–strain curves, analysis of Si–O bonds near the crack tip, and tracking of crack tip position were utilized to quantify the characteristics of crack initiation for quartz in CO_2 environment and to compare these characteristics to those in H_2O and vacuum. These findings were translated in a molecular crack initiation mechanism for quartz in CO_2 environment. Finally, to connect these results to macroscopic quantities, the fracture toughness was evaluated based on the stress intensity factor and compared to experimental data.

3.1. Global Stress–Strain Curves

The global stress–strain curves for the three different environments are shown in Figure 2. When considering the samples that are strained at a rate of 3.4×10^7 s^{-1}, at low strain, quartz samples exhibit similar stress levels in all three environments. However, as the applied strain increases, two distinct behaviors are observed. The quartz sample that only experiences mechanical loading in vacuum exhibits a linear relationship between stress and strain until the maximum yield stress is reached and a catastrophic failure occurs. In contrast, both samples that

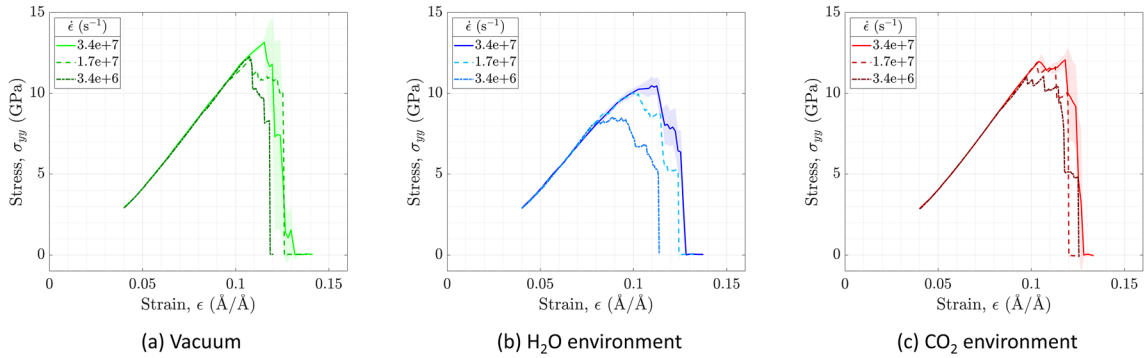

Figure 2. Global stress-strain curves of quartz under tensile mode I loading. Effect of strain rate for quartz sample in (a) vacuum, (b) H_2O, and (c) CO_2 environments. Shaded regions regions represent one standard deviation based on three replica simulations.

are mechanically loaded in a fluid environment show an episodic growth behavior. This behavior is due to early bond breaking in the sample at a lower applied strain. Therefore the samples in these simulations never reach the high yield stress of the mechanically loaded sample in vacuum. The CO_2 and the H_2O environments, on average, reduce the maximum yield stress of quartz by 10% and 20%, respectively, compared to the analogous mechanical loading in vacuum. This reduction in yield stress has previously been reported both computationally and experimentally for stress corrosion cracking in aqueous or damp environments; however, our results suggest that nonpolar fluids, such as CO_2, can impact the mechanical integrity of quartz in a similar manner.

Across all three environments, lower strain rates lead to a decrease in the yield stress (Figure 2). This behavior stems from the longer time of applied strain on the sample. In these cases, the simulation time increased in proportion to the reduction in strain rate. During these long simulations, rare events such as bond breaking can be observed more commonly. While the Si–O bonds on the crack surface have more time to relax and adapt to the applied strain, the process zone grows and affects more bonds in the sample. This scenario is supported by the notion that a catastrophic failure only occurs when a certain strain threshold is reached. Importantly, while these early bond-breaking events lower the yield stress of the material, they do not lead to an earlier formation of a running crack. Typically, these cascading events break a few bonds, followed by a stress build-up period. Hence, the stress–strain curves in Figure 2 show an episodic growth behavior at lower strain rates.

3.2. Si–O Bond Length Analysis

To understand the origin of the yield stress reduction, we analyzed the evolution of the quartz structure. For each of the three environments, the average Si–O bond length is plotted in Figure 3a as a function of distance from the crack tip. As the sample is strained the Si–O bonds elongate throughout the quartz crystal. The most significant

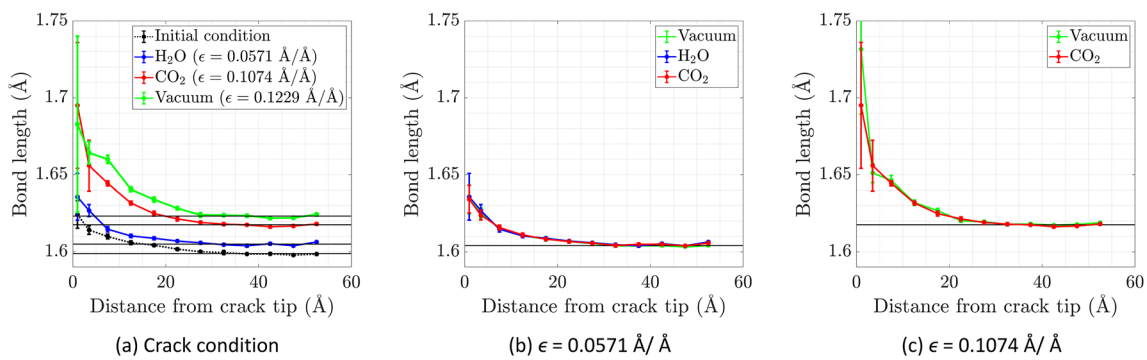

Figure 3. Si–O bond length as a function of distance from the crack tip. (a) Bond-length profiles at the time of first bond-breaking event in each sample. Dotted line represents initial condition as observed at the end of equilibration period. Comparison of bond-length profiles among different environments at the time of first bond-breaking event in (b) H_2O-loaded quartz sample and (c) CO_2-loaded quartz sample. The black lines represent the far-field Si–O bond length is each sample. These results are obtained with an applied strain rate, $\dot{\epsilon} = 3.4 \times 10^7$ s^{-1}.

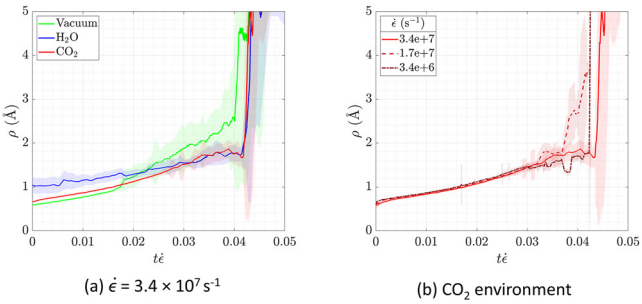

Figure 4. Radius of curvature of the crack tip evolves as applied strain increases. (a) Effect of the fluid environment on the crack tip radius is shown for a strain rate of $\dot{\epsilon} = 3.4 \times 10^7$ s^{-1}. (b) Effect of the strain rate for a quartz sample in CO_2 environment. Solid lines represent moving average of the data.

elongation is observed near the crack tip. Yet, the elongation behavior differs substantially between the three environments. For the aqueous environment, the first bond breaks at a very low applied strain when the Si–O bonds near the crack tip are not any longer than they were initially. This crack initiation at an insignificant mechanical strain suggests that reactivity between the water molecules and the crack surface is the probable cause for the broken bonds in this sample. The vacuum and CO_2 environments exhibit significant bond elongation in contrast to the aqueous environment. Bonds near the crack tip in both these samples reach length approximately 5% greater than that of a relaxed Si–O bond in quartz.

For a quantitative comparison, in Figures 3b and 3c, the average Si–O bond length is plotted as a function of distance from the crack tip at the same strain condition when the first crack growth is observed in the H_2O and CO_2 environments. Indeed, at $\epsilon = 0.0571$ Å/Å, when the first bond breaks in the H_2O environment, the bond profile is comparable among the three environments. This similarity confirms that the mechanical loading is not the key factor to the bond breaking processes in aqueous environments. At the crack condition in the CO_2 environment ($\epsilon = 0.1074$ Å/Å), a finite shoulder is observed in the bond profile at 5 Å away from the crack tip. These elongated bonds inside the process zone are first to break and control further crack growth.

3.3. Crack Tip Radius and Propagation Speed

In this section, we examine the shape of the crack tip and, by tracking the crack tip location, evaluate the crack growth speed. Pook (2000) theoretically derived the crack profile for mode I tensile loading and showed that this profile obtains the form of a parabola. This analytical solution suggests that both the crack length and the crack surface area increase as load is applied. Because the crack tip radius is related to mechanical properties of the material, we characterized how the CO_2 environment affects the evolution of the crack tip. First, using the α-shape method as implemented in OVITO (Stukowski, 2014), the surface atoms on the quartz sample were identified. In adapting the α-shape method, a probe with radius of 2.5 Å was used. Then, the locations of atoms on the crack surface in the near-tip region were fitted to a parabola:

$$f(y) = ay^2 + by + c. \tag{2}$$

From the expression of a parabola, the radius of curvature, ρ, at the crack tip was calculated as (Taneja, 2010):

$$\rho = \left.\frac{\left[1 + f'(y)^2\right]^{3/2}}{f''(y)}\right|_{y=y_{\text{tip}}} = \frac{1}{2a}. \tag{3}$$

Here, the location of the crack tip, y_{tip}, was found by finding the parabola minimum: $f'(y_{\text{tip}}) = 0$. The crack tip radius of curvature that was calculated from the MD trajectory data is shown in Figure 4. Initially, for each of the three environments, the quartz sample, which was loaded at a rate of 3.4×10^7 s^{-1}, shows similar evolution of the crack tip radius. However, the rate of growth at which the radius of curvature of the dry sample evolves increases and exceeds the growth rate of the radii for the samples in CO_2 and H_2O environments. On one hand, this high rate at which the crack tip radius grows in vacuum leads to the significant elongation of the crack tip bonds as shown in Figure 3. On the other hand, the physisorption of fluid molecules on the crack surface leads to bond relaxation and slows down the evolution of the crack tip radius. These results are in agreement with the observations of Rimsza et al. (2018a) for combined chemo-mechanical loading of amorphous silica in an aqueous environment. The sharper crack tip in the fluid environment is a short-time stage in the crack initiation before significant hydrolysis occurs in the high-stress process zone. For the range of strain rates explored in the current study, the strain rate does not substantially affect the crack tip radius, as shown in Figure 4b.

Further, we analyzed the relative crack growth speed among the three environments. For this analysis, we assumed an atomistic crack tip where a single atom represents the tip location. The initial location was known from the simulation setup. For each subsequent step, considering only surface atoms within a 10 Å × 10 Å region around

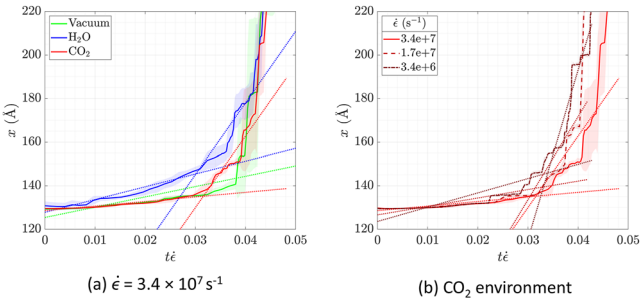

Figure 5. Evolution of crack tip position as a function of applied strain. (a) Effect of fluid environment on crack tip position is shown for a strain rate of $\dot{\epsilon} = 3.4 \times 10^7$ s^{-1}. (b) Effect of the strain rate for a quartz sample in CO_2 environment. Solid and dashed lines represent moving average of the data. Dotted lines represent linear fits to subcritical growth stage and running crack stage.

the crack tip at the previous time step, we identified the surface atom that was farthest from the fluid reservoir and assigned this atom as the new crack tip location. This method is limited by the probe size in the α-shape method and is inherently sensitive to atomistic oscillations. However, its accuracy was found to be satisfactory for the present study. A similar method was employed by Wilson et al. (2019) for tracking the crack tip in molecular simulations of amorphous silica.

To find the crack speed, we analyzed the time-evolving position of the crack tip, which is plotted in Figure 5. In this analysis, the crack speed was calculated from all position data points until the crack tip reaches the end of the sample approximately $\Delta x = 9.5$ nm away from its original location. Using only the x-coordinate in calculating the propagation speed is justified, because, at the nanoscale, the crack propagates straight in the direction of the pre-existing crack (see Figure S6 in Supporting Information S1 for snapshots of the system after the crack has propagated through the sample). The slope of a linear regression to the crack tip position was taken as the propagation speed. Two distinct regimes were identified for the subcritical crack growth: a steady-growth regime with a low propagation speed and an episodic-growth regime with an enhanced propagation speed. The steady subcritical growth regime typically propagates by breaking a few bonds at any given step. In contrast, the episodic-growth regime exhibits a stair-like behavior where slow growth is interspersed with bursts of short traveling cracks.

The effect of the fluid environment on the crack propagation speed is substantial. Notably, the subcritical crack growth rate in the steady regime is 1.84 m/s in an aqueous environment, 1.61 m/s in a vacuum, and only 0.72 m/s in a CO_2 environment. The most notable change is in the episodic-growth regime where running cracks travel through the sample. At the highest strain rate studied here, $\dot{\epsilon} = 3.4 \times 10^7$ s^{-1}, the sample in vacuum skips this regime and transitions directly from the steady subcritical growth regime to a single running crack that leads to catastrophic failure. Both systems that are in fluid environments have an extensive episodic growth regime, where the sample in the aqueous environment shows a propagation speed that is approximately double the crack growth speed in the CO_2 environment. This finding implies that the initiation mechanism for the two fluids is based on distinctly different processes, as discussed in the next section.

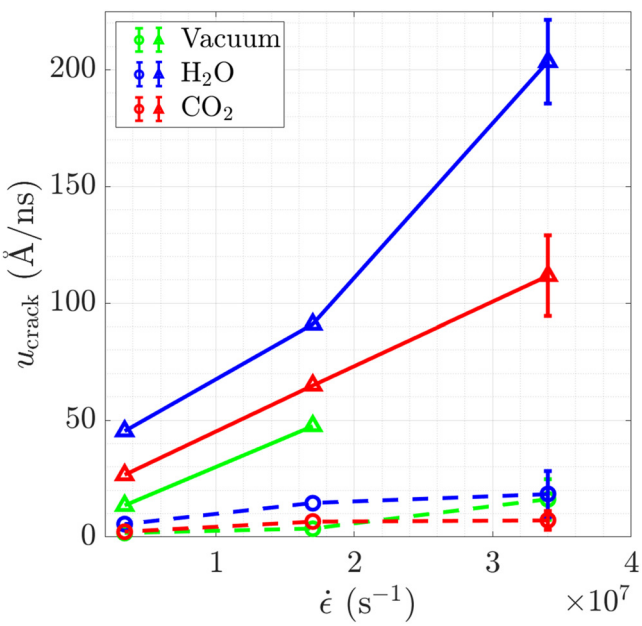

Figure 6. Crack speed in the x-direction as a function of applied strain rate and environment. Circles and dashed lines represent speed in the steady-growth regime, while triangles and solid lines represent speed in the episodic-growth regime. The lines are guide to the eye. Cracks in H_2O, on average, propagate faster than cracks in CO_2 or vacuum. The crack propagation velocity decreases at lower applied strain rates.

Finally, we considered the effect of strain rate on the propagation speed. While the fundamental mechanism for crack initiation in a given environment does not strongly depend on the applied strain rate, the sample that is being mechanically loaded at a lower rate further relaxes and the stress distribution in the process zone is localized near the crack tip. Therefore, at lower strain rates, both the steady subcritical growth and the episodic-growth regimes of crack propagation were observed in all three fluid environments. For CO_2, Figure 5b shows the position of the crack tip as a function of time at each of the three studied strain rates. Once the samples transition into the episodic-growth regime, the crack propagation speed depends on the applied strain rate. The sample that is loaded at the lowest strain rate experiences a crack that grows almost two times slower in the episodic-growth regime than the crack in the sample that is loaded at the intermediate strain rate (see Figure 6). In the two reference systems (vacuum and H_2O), the propagation speed decreases at lower applied strain rates.

Differences in the crack propagation speed have been observed experimentally as a function of the applied stress intensity factor at both slow (Michalske & Freiman, 1982) and high (Leong et al., 2018) strain rates. In particular, Leong et al. (2018) employed X-ray imaging to measure crack front speeds varying between approximately 70 and 1650 m/s in single-crystal quartz with

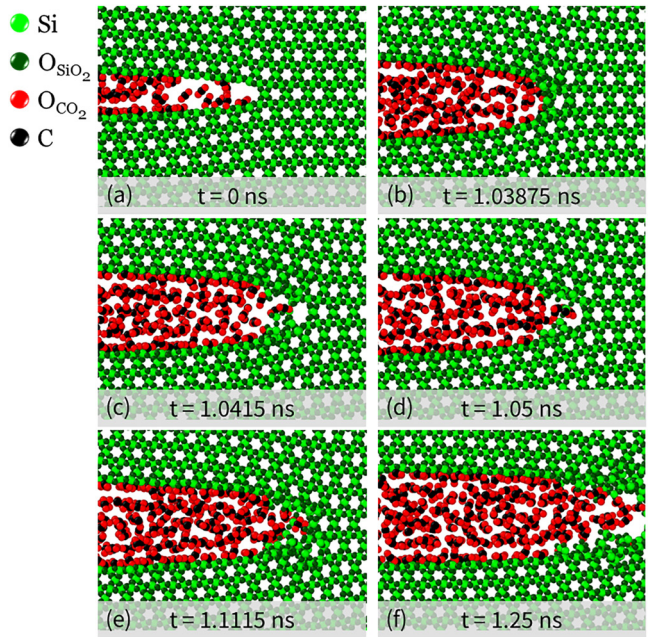

Figure 7. Crack initiation mechanism for quartz in CO_2 environment. Pressure build-up from the physisorbed CO_2 molecules leads to void formation in the process zone. Crack initiation occurs at lower applied strain compared to dry quartz. The atoms are represented with the following color code: Si–light green, O_{SiO_2}–dark green, O_{CO_2}–red, and C–black.

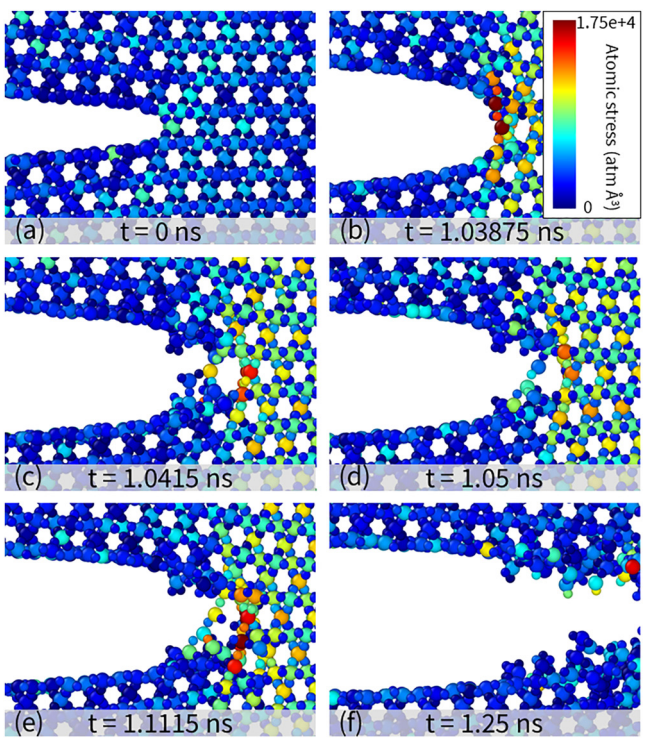

Figure 8. Atomic stress field during crack initiation in quartz in CO_2 environment. Panels correspond to snapshots in Figure 7. Fluid molecules are not shown for clarity. Coloring of atoms represents the magnitude of experienced stress in *y*-direction.

temporal resolution of 153 ns. Considering the distance traveled by the crack tip in the dry quartz sample (green curve in Figure 5a) between $t\dot{\epsilon} = 0.038$ and 0.042, a crack speed of ~65 m/s is obtained, which is in good agreement with experimental results. However, in the current work, because we defined propagation speed as the slope of the crack tip position over time, the effective propagation speed is reported. Therefore, the values shown in Figure 6 are significantly lower. We were able to measure this dynamic propagation speed during the fracturing process, because the reactive simulations provide atomistic resolution of the crack tip, which is inaccessible to state-of-the-art experimental studies (Leong et al., 2018).

3.4. Crack Initiation Mechanism

The trajectory analysis of the crack-tip atoms revealed that the fluid environment significantly influences the speed of crack growth. Furthermore, the investigation of the Si–O bond length near the crack tip showed that the elongation is only one of the processes that lead to bond breaking and crack initiation. Hence, in this section the crack initiation mechanism in CO_2 environments is studied in comparison to the crack initiation mechanisms in vacuum and H_2O environments. For the vacuum environment (see Supporting Information and Figure S5 in Supporting Information S1), void formation controls crack propagation leading to enhanced surface roughness with many dangling bonds (Figure S6 in Supporting Information S1). For the H_2O environment (see Supporting Information and Figure S7 in Supporting Information S1), the polarity leads to breaking of strained Si–O bonds and smooth crack surfaces that are terminated with hydroxyl groups.

The crack initiation mechanism of quartz in CO_2 environments is depicted in Figure 7. When the quartz surface is exposed to CO_2, fluid molecules physisorb on the surface (Figure 7a) and effectively creates a lubrication layer that enables rapid transport of fluid from the reservoir to the crack tip. These physisorbed CO_2 molecules on the crack surface limit the Si–O bond elongation and contribute to pressure build-up in the process zone surrounding the crack (Figure 8). The inhibition of surface bond elongation occurs due to significant interactions involving charge transfer between the physisorbed CO_2 molecules and the quartz surface (see Figure S8 in Supporting Information S1). The pressure build-up inside the quartz sample enhances bond elongation in the process zone (Figure 7b). This process can be noted in Figure 3c, where Si–O bonds located 5 to 10 Å away from the crack tip in the CO_2-loaded sample are as long as or longer than those in the dry sample. Simultaneously, the Si–O bonds on the crack surface are significantly shorter in the CO_2-loaded sample than those belonging to the sample in vacuum.

To quantify the energy of physisorption, we performed first-principles calculations (see Supporting Information S1 for details). These calculations confirmed that the interaction between CO_2 and the solid substrate can be classified as physisorption. The adsorption energy of CO_2 above the (001) surface of SiO_2 is −0.067 eV, a value that agrees with results from literature (Malyi et al., 2015). Because CO_2 is less reactive than water, its physisorption is incapable of dissociating the strained crack tip bonds. Hence, a process similar to that observed for the sample in vacuum unfolds: voids form first inside the process zone (Figure 7c) and create large gaps into which the linear CO_2 molecules diffuse. This diffusion depends on the existence of voids because the large kinetic diameter of CO_2 (330 p.m.) allows fluid molecules to enter the quartz structure only after voids form. Transport of CO_2 into the

Table 1
Fracture Toughness of Quartz for Three Different Environments When the Sample Is Mechanically Loaded in Tensile Mode I With Different Applied Strain Rates

	Fracture toughness, K_{IC} (MPa m$^{1/2}$)		
Fluid	$\dot{\epsilon} = 3.4 \times 10^7$ s^{-1}	$\dot{\epsilon} = 1.7 \times 10^7$ s^{-1}	$\dot{\epsilon} = 3.4 \times 10^6$ s^{-1}
Vacuum	2.81 ± 0.22	2.19	2.48
H_2O	1.04 ± 0.09	0.97	0.86
CO_2	2.47 ± 0.06	2.45	2.27

crystal differs from that of water; H_2O molecules (kinetic diameter of 265 pm.) diffuse into the strained quartz structure before voids form. The diffused CO_2 molecules physisorb on surface sites within the void leading to pressure build-up deeper in the process zone and, eventually, a running crack travels through the sample. Until the critical strain is reached, the crack growth happens in bursts on the order of a nanometer (see Figure 5), which translates to the episodic-growth behavior observed in the global stress–strain curve (Figure 2).

Similarly to the reference environments explored in this paper, the crack initiation mechanism in the CO_2 environment remains invariant with applied strain rate. In the CO_2 environment, the unique difference is that lower strain rates reduce the effective yield stress in a diminishing manner. This limited effect of strain rate on yield stress is because physisorbed CO_2 molecules on the crack surface have the same effect in relaxing the process zone as the effect that is achieved by a lower strain rate in the vacuum environment. Because pressure build-up is a key step of this crack initiation mechanism and the crack radius remains invariant to strain rate, further pressure build-up at the crack front is spatially constrained at lower strain rates; thus, the overall impact on the effective yield stress is limited.

3.5. Fracture Toughness

The fracture toughness in MD data was determined from the stress intensity factor at the instance of the first bond-breaking event (Rimsza et al., 2018a). To calculate the stress intensity factor, Equation 1 was used. This expression was verified numerically to have accuracy within 0.5% for finite samples where $l_c/l_s \leq 0.6$ (Tada et al., 2000), which is the regime of the samples investigated in this work.

The stress intensity factor is proportional to the global stress–strain curves in Figure 2. As the applied strain increased, we observed a monotonic increase in the stress intensity factor. The computed fracture toughness for the three environments is summarized in Table 1. At low strain rate, the dry sample has high fracture toughness of 2.48 MPa m$^{1/2}$ because the first bond-breaking event happens immediately before the formation of a running crack that leads to catastrophic failure of the sample. In contrast to this high value, the quartz sample in water yields a low fracture toughness of 0.86 MPa m$^{1/2}$. This sample experienced both mechanical loading from the applied strain rate and chemical loading from hydrolysis reactions on the surface. The first bond-breaking event was a bond dissociated by H_2O molecules on the surface at low applied strain. These interactions with the aqueous environment manifest as change in the slope of Figure 2b. The mechanical loading, however, remains the cause of the running crack that eventually formed in this sample. Finally, the quartz sample in CO_2 environment shows behavior that is between those of the quartz in vacuum and quartz in an aqueous environment. The first bond-breaking event in this sample occurred upon significant bond elongation, that is, significant applied strain. Therefore, the fracture toughness of quartz in CO_2 environment, when strained at a rate of 3.4×10^7 s^{-1}, sees only modest 12.1% reduction compared to that of dry quartz.

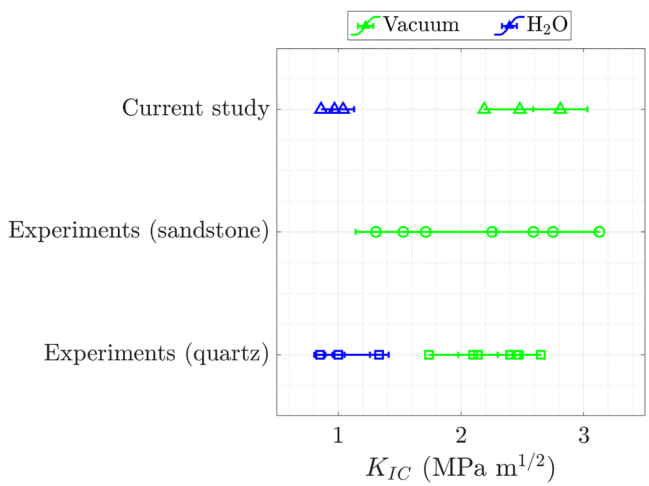

Figure 9. Comparison of fracture toughness obtained from current MD study with experimental measurements for quartz (Atkinson, 1984; Ferguson et al., 1987; Norton & Atkinson, 1981) and sandstone samples (Fuchs, 2017; Kuangsheng et al., 2019) in air/vacuum, and for quartz in liquid water (Atkinson, 1980).

To verify our findings, the fracture toughness values obtained from MD simulations were compared to experiments, based on microscopic and macroscopic measurements (Atkinson, 1984). The reported data shows dependence on a number of environmental factors (e.g., pH factor, temperature, and crystallographic direction). Figure 9 compares published values for fracture toughness of dry and wet quartz to those computed in the present study. The manner in which individual quartz grains fuse together in synthetic quartz compared to the naturally occurring single-crystal mineral leads to difference in the fracture toughness of the two materials. Because of dislocations and impurities, the fracture toughness is lower for fused quartz (or fused silica) and for synthetic quartz than for naturally occurring quartz (Norton & Atkinson, 1981). The fracture toughness of single-crystal quartz in air is

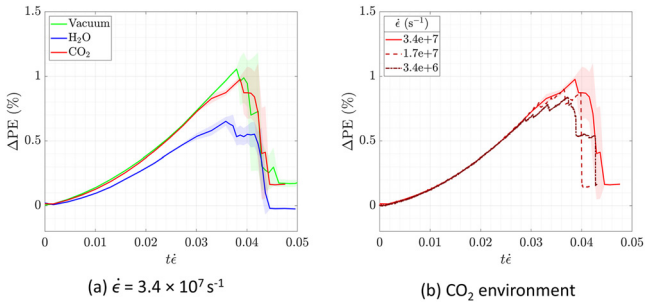

Figure 10. Percent change of total potential energy of the quartz sample during crack initiation. (a) Effect of fluid environment for strain rate of $\dot{\epsilon} = 3.4 \times 10^7$ s^{-1}. (b) Effect of strain rate for the CO_2 environment.

measured to be in the range between 1.74 and 2.65 MPa $m^{1/2}$ (see Figure 9), which is in a good agreement with the computed fracture toughness in the present study. For sandstone, experimental measurements in air have reported fracture toughness of up to 3.12 MPa $m^{1/2}$ (Kuangsheng et al., 2019).

The effect of the fluid environment on the fracture behavior of siliceous materials has been experimentally quantified for air at different humidity levels, liquid water, dry and humid nitrogen, and hydrogen. Additionally, the fracture toughness has been measured in dried samples after aging in various environments, including dry and wet carbon dioxide for a range of pressure and temperature conditions. These experiments suggest that both the aqueous environment and aging within a CO_2 environment reduce the fracture toughness of siliceous materials. In particular, Atkinson (1980) measured the fracture toughness of Arkansas Novaculite (a microcrystaline quartz rock) and two synthetic single crystal quartz samples in liquid water at 20°C. He found these materials to exhibit fracture toughness between 0.852 and 1.335 MPa $m^{1/2}$ in agreement with the fracture toughness calculated in the current MD simulations (see Figure 9). Major et al. (2014) found that the fracture toughness of CO_2-altered Summerville siltstone was lower by 15.5% compared to that of unaltered siltstone from the same formation. This reduction is in a good agreement with our results. Similarly, Sun et al. (2020), who also explored the effects of CO_2 on mechanical properties, found that when exposed to pressurized CO_2 reservoirs at 6–8 MPa for 30 days, the fracture toughness of sandstone decreases by 11.01%–27.89% compared to that of dry sandstone.

Building upon these comparisons between the current results and experimental measurements, we finally discuss the dependence of the fracture toughness on the applied strain rate. As shown in Table 1, lowering the applied strain rate leads to a reduction in the measured fracture toughness. This reduction originates from the additional time available to the process zone to relax. The relaxation in the process zone leads to concentration of the highest stress at the crack front and allows for early breaking of the most strained bonds. Furthermore, this process decreases the energy dissipation via heat release and inelastic deformation. The contributions to the decrease in energy dissipation, G_{diss}, can be traced to the effects of reduced surface roughness, as discussed in the Supporting Information S1, and the related limited change in potential energy, ΔPE, for the quartz sample (Figure 10). This decrease in ΔPE comes from the lack of dangling bonds on the surface.

The fracture toughness of quartz in high-pressure fluid environments that we calculated here is a key result that can directly be used in continuum-scale simulations of geomechanical processes. Its variation with the strain rate can further be used to inform the design principles for enhanced gas recovery and geologic carbon storage in the subsurface.

3.6. Limitations

The assumptions that we made in modeling of the system incur several limitations. Most importantly, the system under consideration is a simplified model of real-life processes in two important ways: (a) we considered pure CO_2 fluid, while in subsurface reservoirs, dissolved CO_2 in brine among other ions is commonly found (Benson & Cole, 2008); (b) only the impact on single-crystal quartz was examined here, while shale rock consists of many minerals, clays, and organic compounds, including amorphous and polycrystalline materials (Jew et al., 2022). Furthermore, future work should examine the influence of carbon dioxide on the crack growth behavior in different crystallographic directions of quartz. These simplifications were necessary due to the computational cost of reactive MD simulations and the availability of accurate force field to model the atomistic interactions, which remains an open area of research. Despite these differences, our model system provides important insight into an understudied process of how non-polar fluids impact the crack initiation in quartz.

4. Conclusion

We studied crack initiation in quartz with reactive MD simulations. Primarily, the corrosive influence of the CO_2 fluid environment and the applied strain rate were investigated and compared to aqueous and vacuum environments. The fluid environments were at high pressure of 100 atm to replicate representative subsurface reservoir

conditions. We proposed a crack initiation mechanism in the CO_2 environment, where individual fluid molecules physisorb on the crack surface, leading to pressure build-up at the crack tip and, hence, to formation of voids inside the quartz crystal at low applied strain. Specifically, the results presented here demonstrate that the fluid environment has a substantial impact on the crack geometry and propagation speed. The differences between the crack initiation mechanism in the CO_2 environment and in the H_2O environment can be summarized as follows:

- Because H_2O molecules have a strong dipole moment, they dissociate during their reaction with quartz and hydroxylate the newly created crack surfaces. In contrast to this behavior, CO_2 molecules do not dissociate upon breaking the Si–O–Si bridges.
- Because the reaction between H_2O molecules and the quartz crack front is not governed by stress level, Si–O–Si bridges break at lower stress in H_2O environment than in CO_2 environment. This difference leads to the lower fracture toughness of quartz in H_2O environment than in CO_2 environments.
- Charge transfer between physisorbed CO_2 molecules and atoms of the quartz crystal near the crack front leads to further stress build-up in the quartz sample and additional elongation of Si–O bonds 5 to 10 Å ahead of the crack front. This elongation leads to void formation at low stress. Such bond stretching was not observed in the H_2O environment.

The corrosive influence of fluids is especially significant at high applied strain rates. At the highest rate investigated in this work, $\dot{\epsilon} = 3.4 \times 10^7\ s^{-1}$, the presence of carbon dioxide leads to reduction in the yield stress of 10%. In contrast to the yield stress, the fracture toughness shows a greater dependence on the fluid environment. Specifically, in aqueous environments, the fracture toughness decreases by 63% due to the chemical reactivity of water with the strained Si–O bonds. In the CO_2 environment, the fracture toughness decreases by only 12.1% due to the pressure build-up near the crack tip. The observed trends in weakened material properties persist across an order of magnitude decrease in the applied strain rate, despite the effect of the fluid environment quantitatively diminishing. At these lower straining rates, the crack initiation timescale is slower than the relaxation timescale, allowing the quartz crystal to relax and the stress field to concentrate near the crack tip. This relaxation of the process zone also leads to the creation of smoother, newly created surfaces because surface reconstruction occurs as the crack propagates through the sample. We thus found that the corrosive influence of the CO_2 fluid environment is important to consider at all applied strain rates, including subcritical crack growth that is typical for the subsurface.

Data Availability Statement

The molecular dynamics data is available through the Stanford Digital Repository at: https://doi.org/10.25740/ch545gn8760. This data includes the complete atomistic trajectories and thermodynamic output files. The Supporting Information contains description of the crack initiation mechanisms for quartz in vacuum and in H_2O environment, computational details for the *ab initio* simulations of CO_2 adsorption on quartz; and, statistical evidence for charge transfer between CO_2 molecules and the surface atoms in the quartz sample.

Acknowledgments
The authors are grateful to Dr. Alireza Ostadhossein for preliminary simulations and helpful discussions. This work was supported as part of the Center for Mechanistic Control of Unconventional Formations (CMC-UF), an Energy Frontier Research Center funded by the U.S. Department of Energy, Office of Science under DOE (BES) Award DE-SC0019165. MI acknowledges support from the Mercator Fellowship (SPP1980) and the Alexander von Humboldt Foundation. The authors are grateful for the resources at the National Energy Research Scientific Computing Center that were utilized for this work.

References

Aktulga, H. M., Fogarty, J. C., Pandit, S. A., & Grama, A. Y. (2012). Parallel reactive molecular dynamics: Numerical methods and algorithmic techniques. *Parallel Computing*, *38*(4–5), 245–259. https://doi.org/10.1016/j.parco.2011.08.005

Atkinson, B. K. (1980). Stress corrosion and the rate-dependent tensile failure of a fine-grained quartz rock. *Tectonophysics*, *65*(3), 281–290. https://doi.org/10.1016/0040-1951(80)90078-5

Atkinson, B. K. (1984). Subcritical crack growth in geological materials. *Journal of Geophysical Research: Solid Earth*, *89*(B6), 4077–4114. https://doi.org/10.1029/JB089iB06p04077

Atkinson, B. K., & Meredith, P. G. (1981). Stress corrosion cracking of quartz: A note on the influence of chemical environment. *Tectonophysics*, *77*(1), T1–T11. https://doi.org/10.1016/0040-1951(81)90157-8

Atkinson, B. K., & Meredith, P. G. (1987). The theory of subcritical crack growth with applications to minerals and rocks. In B. K. Atkinson (Ed.), *Fracture mechanics of rock* (pp. 111–166). Academic Press. https://doi.org/10.1016/B978-0-12-066266-1.50009-0

Barsotti, E., Tan, S. P., Saraji, S., Piri, M., & Chen, J.-H. (2016). A review on capillary condensation in nanoporous media: Implications for hydrocarbon recovery from tight reservoirs. *Fuel*, *184*, 344–361. https://doi.org/10.1016/j.fuel.2016.06.123

Benson, S. M., & Cole, D. R. (2008). CO_2 sequestration in deep sedimentary formations. *Elements*, *4*(5), 325–331. https://doi.org/10.2113/gselements.4.5.325

Bruns, S., Petho, L., Minnert, C., Michler, J., & Durst, K. (2020). Fracture toughness determination of fused silica by cube corner indentation cracking and pillar splitting. *Materials & Design*, *186*, 108311. https://doi.org/10.1016/j.matdes.2019.108311

Chermak, J. A., & Schreiber, M. E. (2014). Mineralogy and trace element geochemistry of gas shales in the United States: Environmental implications. *International Journal of Coal Geology*, *126*, 32–44. https://doi.org/10.1016/j.coal.2013.12.005

Chowdhury, S. C., Haque, B. Z. G., & Gillespie, J. W. (2016). Molecular dynamics simulations of the structure and mechanical properties of silica glass using ReaxFF. *Journal of Materials Science*, *51*(22), 10139–10159. https://doi.org/10.1007/s10853-016-0242-8

Coasne, B., Galarneau, A., Pellenq, R. J. M., & Di Renzo, F. (2013). Adsorption, intrusion and freezing in porous silica: The view from the nanoscale. *Chemical Society Reviews*, *42*(9), 4141–4171. https://doi.org/10.1039/C2CS35384A

Cowen, B. J., & El-Genk, M. S. (2016). Bond-order reactive force fields for molecular dynamics simulations of crystalline silica. *Computational Materials Science*, *111*, 269–276. https://doi.org/10.1016/j.commatsci.2015.09.042

Ferguson, C. C., Lloyd, G. E., & Knipe, R. J. (1987). Fracture mechanics and deformation processes in natural quartz: A combined Vickers indentation, SEM, and TEM study. *Canadian Journal of Earth Sciences*, *24*(3), 544–555. https://doi.org/10.1139/e87-053

Fogarty, J. C., Aktulga, H. M., Grama, A. Y., van Duin, A. C. T., & Pandit, S. A. (2010). A reactive molecular dynamics simulation of the silica-water interface. *The Journal of Chemical Physics*, *132*(17), 174704. https://doi.org/10.1063/1.3407433

Fuchs, S. J. (2017). *Geochemical and geomechanical alteration of mt. simon sandstone due to prolonged contact with CO_2-saturated brine during carbon sequestration (Unpublished master's thesis)*. The University of Texas at Austin.

Guren, M. G., Sveinsson, H. A., Malthe-Sørenssen, A., & Renard, F. (2022). Nanoscale damage production by dynamic tensile rupture in α-quartz. *Geophysical Research Letters*, *49*(20), e2022GL100468. https://doi.org/10.1029/2022GL100468

Henry, J., Paquet, J., & Tancrez, J. (1977). Experimental study of crack propagation in calcite rocks. *International Journal of Rock Mechanics and Mining Sciences & Geomechanics Abstracts*, *14*(2), 85–91. https://doi.org/10.1016/0148-9062(77)90200-5

Jew, A. D., Druhan, J. L., Ihme, M., Kovscek, A. R., Battiato, I., Kaszuba, J. P., et al. (2022). Chemical and reactive transport processes associated with hydraulic fracturing of unconventional oil/gas shales. *Chemical Reviews*, *122*(9), 9198–9263. https://doi.org/10.1021/acs.chemrev.1c00504

Kuangsheng, Z., Yanjun, Z., Tongwu, Z., Xiaohu, B., Shun, L., Guangqing, Z., & Yuanxun, N. (2019). Investigation of supercritical CO_2 effect on fracture toughness of tight sandstone containing weak planes (ARMA-2019-1759).

LAMMPS Manual. (2022). Computer software manual. Retrieved from http://lammps.sandia.gov

Laubach, S. E., Lander, R. H., Criscenti, L. J., Anovitz, L. M., Urai, J. L., Pollyea, R. M., et al. (2019). The role of chemistry in fracture pattern development and opportunities to advance interpretations of geological materials. *Reviews of Geophysics*, *57*(3), 1065–1111. https://doi.org/10.1029/2019RG000671

Leong, A. F. T., Robinson, A. K., Fezzaa, K., Sun, T., Sinclair, N., Casem, D. T., et al. (2018). Quantitative in situ studies of dynamic fracture in brittle solids using dynamic x-ray phase contrast imaging. *Experimental Mechanics*, *58*(9), 1423–1437. https://doi.org/10.1007/s11340-018-0414-3

Major, J., Eichhubl, P., Dewers, T., Urquhart, A., Olson, J., & Holder, J. (2014). The effect of CO_2-related diagenesis on geomechanical failure parameters: Fracture testing of CO_2-altered reservoir and seal rocks from a natural analog at crystal Geyser, Utah. (ARMA-2014-7463).

Malyi, O. I., Thiyam, P., Boström, M., & Persson, C. (2015). A first principles study of CO_2 adsorption on α-SiO_2 (001) surfaces. *Physical Chemistry Chemical Physics*, *17*(31), 20125–20133. https://doi.org/10.1039/C5CP02279G

Meredith, P. G., & Atkinson, B. K. (1983). Stress corrosion and acoustic emission during tensile crack propagation in Whin Sill dolerite and other basic rocks. *Geophysical Journal International*, *75*(1), 1–21. https://doi.org/10.1111/j.1365-246X.1983.tb01911.x

Michalske, T. A., & Freiman, S. W. (1982). A molecular interpretation of stress corrosion in silica. *Nature*, *295*(5849), 511–512. https://doi.org/10.1038/295511a0

Norton, M., & Atkinson, B. (1981). Stress-dependent morphological features on fracture surfaces of quartz and glass. *Tectonophysics*, *77*(3), 283–295. https://doi.org/10.1016/0040-1951(81)90267-5

Oldenburg, C. M., Pruess, K., & Benson, S. M. (2001). Process modeling of CO_2 injection into natural gas reservoirs for carbon sequestration and enhanced gas recovery. *Energy & Fuels*, *15*(2), 293–298. https://doi.org/10.1021/ef000247h

Plimpton, S. (1995). Fast parallel algorithms for short-range molecular dynamics. *Journal of Computational Physics*, *117*, 1–19. https://doi.org/10.1006/jcph.1995.1039

Pook. (2000). Crack profiles and corner point singularities. *Fatigue and Fracture of Engineering Materials and Structures*, *23*(2), 141–150. https://doi.org/10.1046/j.1460-2695.2000.00249.x

Rahimi-Aghdam, S., Chau, V.-T., Lee, H., Nguyen, H., Li, W., Karra, S., et al. (2019). Branching of hydraulic cracks enabling permeability of gas or oil shale with closed natural fractures. *Proceedings of the National Academy of Sciences*, *116*(5), 1532–1537. https://doi.org/10.1073/pnas.1818529116

Raja, V. S., & Shoji, T. (2011). *Stress corrosion cracking: Theory and practice*. Woodhead Publishing.

Rimsza, J. M., Jones, R. E., & Criscenti, L. J. (2018a). Chemical effects on subcritical fracture in silica from molecular dynamics simulations. *Journal of Geophysical Research: Solid Earth*, *123*(11), 9341–9354. https://doi.org/10.1029/2018JB016120

Rimsza, J. M., Jones, R. E., & Criscenti, L. J. (2018b). Crack propagation in silica from reactive classical molecular dynamics simulations. *Journal of the American Ceramic Society*, *101*(4), 1488–1499. https://doi.org/10.1111/jace.15292

Stukowski, A. (2014). Computational analysis methods in atomistic modeling of crystals. *JOM*, *66*(3), 399–407. https://doi.org/10.1007/s11837-013-0827-5

Sun, Z.-d., Song, X.-M., Feng, G., Huo, Y.-m., Wang, Z.-L., & Kong, S.-q. (2020). Influence of supercritical, liquid, and gaseous CO_2 on fracture behavior in sandstone. *Energy Science & Engineering*, *8*(11), 3788–3804. https://doi.org/10.1002/ese3.736

Tada, H., Paris, P. C., & Irwin, G. R. (2000). Stress analysis results for common test specimen configurations. In *The stress analysis of cracks handbook* (3rd ed.). ASME Press. https://doi.org/10.1115/1.801535.ch2

Taneja, H. C. (2010). *Advanced engineering mathematics*. International Publishing House Private Limited.

Taron, J., & Elsworth, D. (2009). Thermal–hydrologic–mechanical–chemical processes in the evolution of engineered geothermal reservoirs. *International Journal of Rock Mechanics and Mining Sciences*, *46*(5), 855–864. https://doi.org/10.1016/j.ijrmms.2009.01.007

Vo, T., He, B., Blum, M., Damone, A., & Newell, P. (2020). Molecular scale insight of pore morphology relation with mechanical properties of amorphous silica using ReaxFF. *Computational Materials Science*, *183*, 109881. https://doi.org/10.1016/j.commatsci.2020.109881

Vo, T., Reeder, B., Damone, A., & Newell, P. (2020). Effect of domain size, boundary, and loading conditions on mechanical properties of amorphous silica: A reactive molecular dynamics study. *Nanomaterials*, *10*(1), 54. https://doi.org/10.3390/nano10010054

Wiederhorn, S. M., & Bolz, L. H. (1970). Stress corrosion and static fatigue of glass. *Journal of the American Ceramic Society*, *53*(10), 543–548. https://doi.org/10.1111/j.1151-2916.1970.tb15962.x

Wilson, M. A., Grutzik, S. J., & Chandross, M. (2019). Continuum stress intensity factors from atomistic fracture simulations. *Computer Methods in Applied Mechanics and Engineering*, *354*, 732–749. https://doi.org/10.1016/j.cma.2019.05.050

Yue, Y., & Zheng, K. (2014). Strong strain rate effect on the plasticity of amorphous silica nanowires. *Applied Physics Letters*, *104*(23), 231906. https://doi.org/10.1063/1.4882420

Zhang, R., Yin, X., Winterfeld, P. H., & Wu, Y.-S. (2016). A fully coupled thermal-hydrological-mechanical-chemical model for CO_2 geological sequestration. *Journal of Natural Gas Science and Engineering*, *28*, 280–304. https://doi.org/10.1016/j.jngse.2015.11.037

References From the Supporting Information

Blöchl, P. E. (1994). Projector augmented-wave method. *Physical Review B*, *50*(24), 17953–17979. https://doi.org/10.1103/PhysRevB.50.17953

Cygan, R. T., Liang, J.-J., & Kalinichev, A. G. (2004). Molecular models of hydroxide, oxyhydroxide, and clay phases and the development of a general force field. *The Journal of Physical Chemistry B*, *108*(4), 1255–1266. https://doi.org/10.1021/jp0363287

Deng, L., Miyatani, K., Suehara, M., Amma, S.-i., Ono, M., Urata, S., & Du, J. (2021). Ion-exchange mechanisms and interfacial reaction kinetics during aqueous corrosion of sodium silicate glasses. *npj Materials Degradation*, *5*(1), 15. https://doi.org/10.1038/s41529-021-00159-4

Grimme, S., Antony, J., Ehrlich, S., & Krieg, H. (2010). A consistent and accurate ab initio parametrization of density functional dispersion correction (dft-d) for the 94 elements h-pu. *The Journal of Chemical Physics*, *132*(15), 154104. https://doi.org/10.1063/1.3382344

Jain, A., Ong, S. P., Hautier, G., Chen, W., Richards, W. D., Dacek, S., et al. (2013). Commentary: The materials project: A materials genome approach to accelerating materials innovation. *APL Materials*, *1*(1), 011002. https://doi.org/10.1063/1.4812323

Kresse, G., & Furthmüller, J. (1996). Efficient iterative schemes for ab initio total-energy calculations using a plane-wave basis set. *Physical Review B*, *54*(16), 11169–11186. https://doi.org/10.1103/PhysRevB.54.11169

Mohammed, S., Sunkara, A. K., Walike, C. E., & Gadikota, G. (2021). The role of surface hydrophobicity on the structure and dynamics of CO_2 and CH_4 confined in silica nanopores. *Frontiers in Climate*, *3*, 713708. https://doi.org/10.3389/fclim.2021.713708

Momma, K., & Izumi, F. (2011). *VESTA3* for three-dimensional visualization of crystal, volumetric and morphology data. *Journal of Applied Crystallography*, *44*(6), 1272–1276. https://doi.org/10.1107/S0021889811038970

Monkhorst, H. J., & Pack, J. D. (1976). Special points for brillouin-zone integrations. *Physical Review B*, *13*(12), 5188–5192. https://doi.org/10.1103/PhysRevB.13.5188

Perdew, J. P., Burke, K., & Ernzerhof, M. (1996). Generalized gradient approximation made simple. *Physical Review Letters*, *77*(18), 3865–3868. https://doi.org/10.1103/PhysRevLett.77.3865

Persson, K. (2014). Materials data on SiO_2 (sg:154) by Materials Project. https://doi.org/10.17188/1272701

Potoff, J. J., & Siepmann, J. I. (2001). Vapor–liquid equilibria of mixtures containing alkanes, carbon dioxide, and nitrogen. *AIChE Journal*, *47*(7), 1676–1682. https://doi.org/10.1002/aic.690470719

Smith, D. L., & Evans, B. (1984). Diffusional crack healing in quartz. *Journal of Geophysical Research*, *89*(B6), 4125–4135. https://doi.org/10.1029/JB089iB06p04125

Xu, S., & Deng, X. (2008). Nanoscale void nucleation and growth and crack tip stress evolution ahead of a growing crack in a single crystal. *Nanotechnology*, *19*(11), 115705. https://doi.org/10.1088/0957-4484/19/11/115705